

PRECISE MASSES IN THE WASP-47 SYSTEM

ANDREW VANDERBURG^{18,1,†,*}, JULIETTE C. BECKER^{2,†}, LARS A. BUCHHAVE³, ANNELIES MORTIER⁴, ERIC LOPEZ⁵, LUCA MALAVOLTA^{6,17}, RAPHAËLLE D. HAYWOOD^{1,*}, DAVID W. LATHAM¹, DAVID CHARBONNEAU¹, MERCEDES LÓPEZ-MORALES¹, FRED C. ADAMS^{2,14}, ALDO STEFANO BONOMO⁸, FRANÇOIS BOUCHY⁷, ANDREW COLLIER CAMERON⁴, ROSARIO COSENTINO⁹, LUCA DI FABRIZIO⁹, XAVIER DUMUSQUE⁷, ALDO FIOREZZANO⁹, AVET HARUTYUNYAN⁹, JOHN ASHER JOHNSON¹, VANIA LORENZI^{9,15,16}, CHRISTOPHE LOVIS⁷, MICHEL MAYOR⁷, GIUSI MICELA¹⁰, EMILIO MOLINARI^{9,13}, MARCO PEDANI⁹, FRANCESCO PEPE⁷, GIAMPAOLO PIOTTO^{6,17}, DAVID PHILLIPS¹, KEN RICE¹¹, DIMITAR SASSELOV¹, DAMIEN SÉGRANSAN⁷, ALESSANDRO SOZZETTI⁸, STÉPHANE UDRY⁷, CHRIS WATSON¹²

ABSTRACT

We present precise radial velocity observations of WASP-47, a star known to host a hot Jupiter, a distant Jovian companion, and, uniquely, two additional transiting planets in short-period orbits: a super-Earth in a ≈ 19 hour orbit, and a Neptune in a ≈ 9 day orbit. We analyze our observations from the HARPS-N spectrograph along with previously published data to measure the most precise planet masses yet for this system. When combined with new stellar parameters and reanalyzed transit photometry, our mass measurements place strong constraints on the compositions of the two small planets. We find unlike most other ultra-short-period planets, the inner planet, WASP-47 e, has a mass ($6.83 \pm 0.66 M_{\oplus}$) and radius ($1.810 \pm 0.027 R_{\oplus}$) inconsistent with an Earth-like composition. Instead, WASP-47 e likely has a volatile-rich envelope surrounding an Earth-like core and mantle. We also perform a dynamical analysis to constrain the orbital inclination of WASP-47 c, the outer Jovian planet. This planet likely orbits close to the plane of the inner three planets, suggesting a quiet dynamical history for the system. Our dynamical constraints also imply that WASP-47 c is much more likely to transit than a geometric calculation would suggest. We calculate a transit probability for WASP-47 c of about 10%, more than an order of magnitude larger than the geometric transit probability of 0.6%.

Subject headings: planets and satellites: detection, planets and satellites: gaseous planets

1. INTRODUCTION

Among the many scientific results from the K2 mission, the discovery of two additional transiting planets in the known hot Jupiter WASP-47 system was perhaps the most surprising. After the second of the *Kepler* space telescope’s four reaction wheels failed and the spacecraft was re-purposed to undertake the K2 mission (Howell et al. 2014), the parade of stunning results from the original *Kepler* mission — from low-density multi-transiting systems (Lissauer et al. 2011), to evaporating and disintegrating sub-Mercury-sized planets (Rappaport et al. 2012), to an abundance of small, likely rocky planets in their host stars’ habitable zones (Dressing & Charbonneau 2013; Petigura et al. 2013a; Burke et al. 2015) — was largely expected to slow. The *Kepler* era of discovery was instead expected to give way to a new era in which the K2 mission would largely find more of the same kinds of planets that had been previously discovered, just orbiting brighter stars or in different environments. While K2 has certainly delivered in that regard, finding small planets around nearby stars well-suited to detailed characterization (Vanderburg et al. 2015; Sinukoff et al. 2016; Vanderburg et al. 2016a; Rodriguez et al. 2017; Crossfield et al. 2017), temperate planets around M-dwarfs (Crossfield et al. 2015; Petigura et al. 2015; Martinez et al. 2017; Dressing et al. 2017a,b), and planets in open clusters (Mann et al. 2016b,a; David et al. 2016; Obermeier et al. 2016; Libralato et al. 2016; Mann et al. 2017), K2 is still delivering new and unexpected discoveries, like the unique architecture of the WASP-47 system, that are yielding fundamental insights about the formation and evolution of planetary systems.

¹ Harvard–Smithsonian Center for Astrophysics, 60 Garden St., Cambridge, MA 02138, USA

² Astronomy Department, University of Michigan, Ann Arbor, MI 48109, USA

³ Centre for Star and Planet Formation, Natural History Museum of Denmark & Niels Bohr Institute, University of Copenhagen, Øster Voldgade 5-7, DK-1350 Copenhagen K.

⁴ Centre for Exoplanet Science, SUPA, School of Physics & Astronomy, University of St Andrews, St Andrews KY16 9SS, UK

⁵ NASA Goddard Space Flight Center, Greenbelt, MD 20771, USA

⁶ Dipartimento di Fisica e Astronomia “Galileo Galilei”, Università di Padova, Vicolo dell’Osservatorio 3, 35122 Padova, Italy

⁷ Observatoire Astronomique de l’Université de Genève, 51 chemin des Maillettes, 1290 Versoix, Switzerland

⁸ INAF – Osservatorio Astrofisico di Torino, Via Osservatorio 20, I-10025 Pino Torinese, Italy

⁹ INAF – Fundación Galileo Galilei, Rambla José Ana Fernández Pérez, 7, 38712 Breña Baja, Spain

¹⁰ INAF – Osservatorio Astronomico di Palermo, Piazza del Parlamento 1, 90124 Palermo, Italy

¹¹ SUPA, Institute for Astronomy, Royal Observatory, University of Edinburgh, Blackford Hill, Edinburgh EH93HJ, UK

¹² Astrophysics Research Centre, School of Mathematics and Physics, Queens University Belfast, Belfast BT7 1NN, UK

¹³ INAF – IASF Milano, via Bassini 15, 20133, Milano, Italy

¹⁴ Physics Department, University of Michigan, Ann Arbor, MI 48109, USA

¹⁵ Instituto de Astrofísica de Canarias, C/ Vía Láctea, s/n, 38205 - La Laguna (Tenerife), Spain

¹⁶ Departamento de Astrofísica, Universidad de La Laguna, Tenerife, Spain

¹⁷ INAF – Osservatorio Astronomico di Padova, Vicolo dell’Osservatorio 5, 35122 Padova, Italy

¹⁸ Department of Astronomy, The University of Texas at Austin, Austin, TX 78712, USA

[†] NSF Graduate Research Fellow

* NASA Sagan Fellow

The WASP-47 planetary system was first discovered by the ground-based Wide Angle Search for Planets (WASP) survey (Hellier et al. 2012). After detecting a candidate hot Jupiter in a 4.16 day orbital period with the WASP-South instrument, Hellier et al. (2012) followed-up the system and confirmed the planetary nature of WASP-47b with a transit observation with the EulerCam photometer and moderate precision radial velocity observations from the CORALIE spectrograph, both on the 1.2m Euler telescope at La Silla Observatory in Chile. Several years later, WASP-47 happened to lie in Field 3 of the K2 mission, and was observed by K2 between November 2014 and February 2015. In addition to the previously known hot Jupiter, the precise K2 photometry revealed two other transiting planets, an interior super-Earth in a 19 hour orbit, and an exterior Neptune-sized planet in a 9 day orbit, making WASP-47 the first and only hot Jupiter system with additional short-period transiting planets (Becker et al. 2015). Meanwhile, long-term radial velocity monitoring of WASP-47 with CORALIE was also revealing interesting trends. Using 48 observations obtained over the course of almost 5 years, Neveu-VanMalle et al. (2016) detected another giant planet orbiting WASP-47 in a nearly 600-day orbit, giving a total of four known planets around WASP-47.

Although in 2015, when WASP-47 c, d, and e were discovered, extra transiting planets in a hot Jupiter system seemed unusual and surprising, such planets were once believed likely to exist, and were in fact seen as a highly promising way to find small transiting planets before the launch of multi-million-dollar wide-field space telescopes like *Kepler* and CoRoT. Holman & Murray (2005) and Agol et al. (2005) showed that a transiting planet would undergo small deviations from perfectly periodic transits (called transit timing variations or TTVs) in the presence of other nearby planets in the system, and Steffen & Agol (2005) showed that this method is highly sensitive to small planets orbiting near hot Jupiters. Frustratingly, however, after a decade of searching, the TTV method’s exquisite sensitivity to small planets near hot Jupiters had merely translated to exquisite upper limits on the presence of such planets (especially in mean motion resonances with the hot Jupiter, Steffen & Agol 2005; Miller-Ricci et al. 2008; Collins et al. 2017).

Meanwhile, shortly after its launch, the *Kepler* telescope detected the first transit timing variations in systems of longer period and lower mass planets than the hot Jupiters on which previous searches had focused (Holman et al. 2010; Lissauer et al. 2011). Over the course of its mission, *Kepler* found planets in nearly every configuration imaginable²¹, including tightly packed systems of small planets with short orbital periods (Muirhead et al. 2012) and multi-planet systems with slightly longer period warm Jupiters (Bonomo et al. 2014; Sanchis-Ojeda et al. 2014; Huang et al. 2016), but *Kepler* found no evidence for any additional planets near a hot Jupiter. When detailed investigations and searches for companions to hot Jupiters in *Kepler* data came up empty (Steffen et al. 2012), the scientific community largely consid-

ered the issue resolved — hot Jupiters evidently either cannot or almost never have nearby planetary companions.

Therefore, the planets around WASP-47 must represent a rare outcome of planet formation, and any observational or theoretical insights into their architecture and origins are important to help illuminate this new mode. Follow-up work came quickly. Sanchis-Ojeda et al. (2015) detected the Rossiter McLaughlin effect for WASP-47b, ruling out large misalignments between the inner transiting system’s orbits and the star’s sky-projected spin axis. Radial velocity monitoring with the Planet Finder Spectrograph (PFS) on the Magellan Clay telescope detected the reflex motion due to WASP-47e and found that its composition was most likely rocky (Dai et al. 2015). More recently, a larger set of precise velocities from the High Resolution Echelle Spectrometer (HIRES) on the Keck I telescope obtained by Sinukoff et al. (2017b) improved the precision on WASP-47e’s mass and detected WASP-47d’s RV signature. A photodynamical analysis by Almenara et al. (2016) and a simultaneous analysis of radial velocities and transit times by Weiss et al. (2016a) placed even stronger constraints on the planets’ masses and eccentricities, showing that WASP-47d had a mass close to that of Neptune, and that the eccentricities of the inner planets were small. Becker & Adams (2017) used the fact that the three inner planets all transit to place constraints on the inclination of WASP-47c. They showed that WASP-47c’s orbit is probably fairly well aligned with the transiting planets, though certain highly misaligned orbits could still allow the inner planets to transit.

Meanwhile, others have speculated about the origin of the WASP-47 planets. Batygin et al. (2016) suggested that *in situ* formation could be an important channel for creating hot Jupiters, and that small planetary companions like those around WASP-47 (or in orbits misaligned with the hot Jupiter) would be a natural consequence of this mechanism. Huang et al. (2016) also suggested *in situ* formation, noting that the planets around WASP-47 are much more reminiscent of planetary systems hosting warm Jupiters than other hot Jupiters, and speculating that WASP-47 might be an extreme short-period result of an *in situ* warm Jupiter formation mechanism. On the other hand, Weiss et al. (2016a) suggested that WASP-47’s planets might have formed in a two-stage process, where the two Jovian planets formed far out in the disk, WASP-47b migrated inwards, and then the two smaller planets formed nearby. More constraints on the planets’ masses and compositions and the system architecture are needed to understand how these unusual planets formed and came to be in their present configuration.

In this paper, we add to the already large body of follow-up work on the WASP-47 system, presenting 69 new precise radial velocity observations from the High Accuracy Radial velocity Planet Searcher for the Northern hemisphere (HARPS-N). We analyze these new observations along with previously collected data to determine the most precise values yet for the masses and radii of the WASP-47 planets. In Section 2, we describe our HARPS-N dataset. Section 3 describes our analysis of the HARPS-N data to measure spectroscopic properties and planet masses, as well as a re-analysis of the K2 light curve, and a re-determination of the host star’s physical

²¹ Some exceptions to this statement include the lack of binary planets, Trojan planets, and circumtrinary planets among *Kepler*’s discoveries.

properties. In Section 4, we use N-body integrations to simulate the WASP-47 system using our new measurements of the planetary masses, and place constraints on the inclination of the long-period, not necessarily transiting planet WASP-47 c. Finally, in Section 5, we discuss what our measurements tell us about the compositions of the WASP-47 planets and what our dynamical constraints tell us about the system’s history.

2. HARPS-N SPECTROSCOPY

We observed WASP-47 with the HARPS-N spectrograph on the 3.58m Telescopio Nazionale Galileo (TNG) on the island of La Palma, Spain (Cosentino et al. 2012). HARPS-N is a stabilized high resolution ($\lambda/\Delta\lambda = 115,000$) optical spectrograph designed specifically to make precise radial velocity measurements. We began observing WASP-47 on 23 July 2015, shortly after K2 data revealed the presence of two small transiting planets (WASP-47 e and WASP-47 d) in addition to the previously known hot Jupiter (WASP-47 b). We obtained 78 observations of WASP-47 with integration times of 30 minutes. We measured radial velocities for each exposure by cross-correlating the HARPS-N spectra with a weighted binary mask (Baranne et al. 1996; Pepe et al. 2002). The 30 minute exposures of WASP-47 yielded radial velocity measurements with typical photon-limited uncertainties of 3 m s^{-1} . HARPS-N is fed by two optical fibers going into the spectrograph - one fiber feeds the target starlight into the spectrograph, while the other fiber either feeds in a precise wavelength calibrator²², or sky background light. HARPS-N is stable to better than 1 m s^{-1} over the course of a night, considerably more precise than our typical measurement uncertainties, so a simultaneous calibrator was not necessary for our observations. Instead, we fed sky background light into the instrument with the second fiber.

Because WASP-47 is somewhat faint for precise radial velocity measurements, and because it lies in the ecliptic plane near bright solar system objects like the moon, contamination from scattered sky background light can cause significant velocity errors in some conditions. We identified radial velocity observations contaminated by scattered light from a bright sky using the method described by Malavolta et al. (2017). In brief, we calculated radial velocities with and without sky contribution removed (using the sky spectrum obtained simultaneously with the instrument’s second fiber), and flagged the exposures that showed a significant ($2\text{-}\sigma$) velocity difference with and without sky subtraction. We found that four of our 78 observations showed evidence for sky contamination and excluded them from our analysis (which we describe in Section 3.4).

3. ANALYSIS

3.1. Spectroscopic Parameters

We used our HARPS-N spectra to measure spectroscopic parameters for WASP-47. We first used the Stellar Parameter Classification (SPC) method (Buchhave et al. 2012, 2014). SPC works by cross-correlating a stellar spectrum with synthetic spectra from Kurucz (1992)

²² The wavelength calibrator light source can be a Thorium Argon lamp, continuum light passed through a stabilized Fabry-Perot interferometer, or a stabilized laser frequency comb.

model atmospheres and interpolating the resulting correlation peaks to determine stellar atmospheric parameters like effective temperature, surface gravity, metallicity, and line broadening. We ran SPC on 75 of the 78 HARPS-N spectra²³ and calculated the averages for all of the spectroscopic parameters. With SPC, we measure a temperature of $T_{\text{eff,SPC}} = 5571 \pm 50 \text{ K}$, a surface gravity of $\log g_{\text{cgs,SPC}} = 4.39 \pm 0.1$, a metallicity $[\text{M}/\text{H}]_{\text{SPC}} = 0.42 \pm 0.08$, and place an upper limit on rotational velocity of $v_{\text{rot}} < 2 \text{ km s}^{-1}$. The error bars reported for SPC reflect systematic uncertainties in the stellar models used by SPC. The scatter in the parameters SPC reports for each of the 75 individual spectra is much smaller than the systematic uncertainty in these parameters.

We also measured spectroscopic parameters using the method described by Mortier et al. (2013) on our new HARPS-N spectra. We co-added all of the HARPS-N spectra, measured equivalent widths of iron lines using ARES2 (Sousa 2014; Sousa et al. 2015), and determined atmospheric parameters using the 2014 version of MOOG²⁴ (Snedden 1973). We then applied the surface gravity correction from Mortier et al. (2014) to adjust for systematic effects in the ARES/MOOG analysis method. This analysis yielded an effective temperature $T_{\text{eff,MOOG}} = 5614 \pm 67 \text{ K}$, surface gravity $\log g_{\text{cgs,MOOG}} = 4.45 \pm 0.11$, and an iron abundance $[\text{Fe}/\text{H}]_{\text{MOOG}} = 0.39 \pm 0.05$.

The spectroscopic parameters that we determined through our SPC and ARES/MOOG analyses are consistent with one another, and are also consistent within errors with previous determinations. In this paper, we adopt weighted averages of the spectroscopic parameters from our SPC analysis and our ARES/MOOG analysis, along with the spectroscopic analysis done by Sinukoff et al. (2017b) on a high signal-to-noise spectrum from Keck Observatory using another independent method, Spectroscopy Made Easy (SME, Brewer et al. 2015, 2016). Each of the three methods we use have their own systematics, so averaging the three methods could give more accurate spectroscopic parameters. The weighted averages were a temperature of $T_{\text{eff}} = 5552 \text{ K}$, a metallicity²⁵ of $[\text{M}/\text{H}] = 0.38$, and a stellar surface gravity of $\log g_{\text{cgs}} = 4.32$. We assigned conservative error bars of 75 K in temperature, 0.05 dex in metallicity, and 0.1 dex in surface gravity to the weighted averages in order to account for systematic errors in the spectroscopic analyses.

3.2. Transit Re-analysis

Since the original analysis of the WASP-47 K2 light curve by Becker et al. (2015), there have been new data collected (Sinukoff et al. 2017b) and additional dynamical analyses (Almenara et al. 2016; Weiss et al. 2016a) performed, which put tighter constraints on the planets’ orbits (in particular, their eccentricities). In this

²³ We excluded several spectra due to their low signal-to-noise ratios. We did not exclude the sky-contaminated spectra from our SPC analysis because the small amount of sky contamination necessary to skew the radial velocity by $\approx 10 \text{ m s}^{-1}$ does not significantly affect the SPC analysis.

²⁴ <http://www.as.utexas.edu/~chris/moog.html>

²⁵ To calculate the weighted average metallicity, we use iron abundance as a proxy for the overall metallicity by assuming solar abundance ratios, where $[\text{M}/\text{H}] = [\text{Fe}/\text{H}]$.

section, we re-analyze the K2 light curve using Kepler’s third law to link together the planets’ scaled semi-major axes while taking into account new, tighter constraints on the inner planets’ orbital eccentricities. These constraints yield better measurements of the planets’ scaled semi-major axes, and therefore better measurements of the planets’ transit impact parameters and planet to star radius ratios.

We performed our new transit analysis using the same K2 light curve of WASP-47 produced and used by Becker et al. (2015). *Kepler* observed WASP-47 for 69 days between 2014 November 14 and 2015 January 23 in short-cadence mode – an exposure of WASP-47 was recorded every 58.85 seconds instead of *Kepler*’s normal 29.4 minute “long cadence” integrations. After Becker et al. (2015) processed the light curve to remove systematic effects due to *Kepler*’s unstable pointing (see also Vanderburg & Johnson 2014; Vanderburg et al. 2016b), the photometric scatter in the light curve was about 350 ppm per minute.

We perform the transit analysis on the K2 light curve using a Markov Chain Monte Carlo (MCMC) algorithm with an affine invariant ensemble sampler (Goodman & Weare 2010). We fit the three transiting planet light curves with Mandel & Agol (2002) model light curves (with a quadratic limb darkening law parameterized following Kipping 2013). We fit for the planets’ orbital periods, transit ephemerides²⁶, planet to star radius ratios (R_p/R_*), orbital inclinations (i), and in some cases, the orbital eccentricity (e) and argument of periastron (ω_p). Instead of fitting for all three planets’ scaled semi-major axis ratios (a/R_*) independently, we fit for stellar density and calculated a/R_* for each planet using Kepler’s third law. We also fit for a single flux offset parameter and the uncertainty of each K2 photometric datapoint.

We force the orbits of WASP-47e and WASP-47b to be circular; the tidal circularization timescales for these two planets (10^5 years and 10^7 years respectively, using the expression from Goldreich & Soter 1966 and reasonable values²⁷ of Q and k_2) are much shorter than the age of the system²⁸. For WASP-47d, while tidal dissipation is not strong enough to necessarily circularize the orbit, strong dynamical constraints exist on any eccentricity. Both N-body simulations performed by Becker et al. (2015) and simultaneous analysis of transit times and radial velocities by Almenara et al. (2016) and Weiss et al. (2016a) have showed that the eccentricity must be quite small. We imposed a half-Gaussian prior on eccentricity centered at 0 with a $1-\sigma$ width of 0.014, and solutions with eccentricity less than 0 forbidden. This prior matches the distribution of dynamically stable simulations from Becker et al. (2015) and gives a $2-\sigma$ upper

²⁶ Even though small transit timing variations have been detected in the K2 light curve, for this analysis, we assumed the transits of the WASP-47 planets are perfectly periodic. We have also analyzed the K2 light curve while shifting the transit center times to account for the transit timing variations, and found the difference in fitted parameters was negligible.

²⁷ In particular, we used $Q/k_2 = 10^2$ for WASP-47e and $Q/k_2 = 10^5$ for WASP-47b and WASP-47d.

²⁸ Planet-planet interactions will drive a small forced eccentricity but our dynamical calculations show that typical forced eccentricities for these planets are of order 10^{-3} , too small to affect our measured parameters.

limit on eccentricity that matches the limit from Weiss et al. (2016a). In our MCMC fit, we explored eccentric models for WASP-47d’s orbit by stepping in $\sqrt{e} \sin \omega_p$ and $\sqrt{e} \cos \omega_p$.

We initialized an ensemble of 100 walkers, evolved them for 20,000 steps, and removed the first 10,000 steps, when the ensemble was “burning in” and not yet in a converged configuration. We assessed convergence of the resulting MCMC chains by calculating the Gelman Rubin statistic, which was less than 1.2 for all parameters, and less than 1.05 for most. The best-fit parameters and their uncertainties are reported in Table 3. The results are consistent with the previous transit analyses by Becker et al. (2015) and Almenara et al. (2016), but in some cases are more precise because of the additional constraints we have imposed here. Thanks to the high signal-to-noise transits of WASP-47b, we measure the stellar limb darkening coefficients²⁹ and importantly, we measure the stellar density with a precision of 1.4%, which we use in Section 3.3 to determine a precise stellar mass and radius. We also measure the radius ratios of WASP-47e and WASP-47d with 0.8% and 0.5% precision, respectively.

3.3. Stellar Parameters

In this section, we take advantage of the well measured stellar density we measure from the K2 transit photometry to derive precise stellar parameters (as has been done previously for other hot Jupiter hosts, e.g. Sozzetti et al. 2007). We base our analysis on the Yonsei-Yale (YY) isochrones (Yi et al. 2001), exploring parameter space stepping in stellar mass, age, and metallicity using MCMC with an affine invariant ensemble sampler. We interpolated the YY isochrones using code³⁰ written by Jason Eastman for EXOFASTv2 (Eastman et al. 2013; Rodriguez et al. 2017; Eastman et al. in prep). We impose Gaussian priors on WASP-47’s density, metallicity, effective temperature, and surface gravity. The density prior’s center and width come from our analysis of the K2 light curve. For the temperature, metallicity, and surface gravity priors, we use the values and uncertainties from the weighted average of the three different spectroscopic analyses we discussed in Section 3.1.

Thanks to our precise measurement of WASP-47’s density from the transit light curves, our MCMC analysis yielded a stellar mass and radius with precisions of about 3% and 1% respectively. Stellar evolutionary models have not yet been tested at such high precisions on stellar parameters (Torres et al. 2010), so we performed tests to assess the scale of systematic errors in the isochrones we used. First, we compared the results of our analysis with the YY isochrones to the similar analysis performed by Almenara et al. (2016) using the Dartmouth isochrones (Dotter et al. 2008). Using the same priors and input stellar parameters, our YY analysis yielded a mass about 1.5% larger and a radius about 0.5% larger than the values Almenara et al. (2016) determined using the Dartmouth isochrones. The differences in mass and

²⁹ We measure the linear coefficient $u_1 = 0.533 \pm 0.010$ and the quadratic coefficient $u_2 = 0.097 \pm 0.024$. These coefficients are in reasonable agreement (within ≈ 0.1) with the theoretical predictions from Claret & Bloemen (2011) of $u_1 = 0.47$ and $u_2 = 0.22$.

³⁰ Code available at <https://github.com/jdeast/EXOFASTv2/>.

radius between the YY analysis and Dartmouth analyses are about half the size of the uncertainties from each analysis. We also performed an MCMC analysis to determine WASP-47's stellar parameters using the empirical mass and radius relations determined by Torres et al. (2010). We stepped in surface gravity, metallicity, and effective temperature, imposing Gaussian priors on the metallicity, temperature, and stellar density. The Torres relations have a known offset at one solar mass, over-predicting the mass of the Sun by about 5% and the radius of the Sun by about 2% (Torres et al. 2010), so we scaled the output masses and radii inside our model by those factors to correct for the offset – forcing the relations to correctly predict the Sun's density. Our analysis using the Torres relations yielded masses and radii that were about 0.7% and 0.1% larger than our analysis using the YY isochrones. These discrepancies again are considerably smaller than the uncertainties we determined in our stellar parameters. Finally, we repeated the analysis with the Torres relations while applying the empirical correction for solar-mass stars provided by Santos et al. (2013), and found that it also gave consistent values for the stellar mass and radius, with values about 0.5- σ larger than the YY value.

Based on these tests showing different models and relations all predicting consistent stellar parameters for WASP-47, we conclude that systematic uncertainties in the stellar masses and radii we derive are small. This makes sense – stellar evolutionary models are calibrated off the Sun and incorporate physics known to be important for Sun-like stars, and therefore tend to be most accurate for stars with parameters close to those of the Sun. WASP-47 has a mass only 4% larger than the sun, and is only slightly more evolved, with a $\approx 14\%$ larger radius and ≈ 200 K cooler stellar effective temperature. The biggest discrepancy between WASP-47 and the Sun is the composition – WASP-47 has a metallicity 2.5 times higher than that of the Sun, which is possibly the cause of the small discrepancies we do see between the different methods.

To take the 0.5- σ discrepancies we found into account, we re-determined the stellar mass and radius using our YY MCMC analysis after inflating the uncertainty on stellar density by adding an 0.5- σ systematic uncertainty in quadrature to the uncertainty we derived from our transit analysis. This analysis yielded a stellar mass of $1.040 \pm 0.031 M_{\odot}$ and a radius of $1.137 \pm 0.013 R_{\odot}$. Our constraint on stellar density is precise enough that we also measure an isochronal age of $6.7^{+1.5}_{-1.1}$ Gyr for WASP-47, although the precision of this age determination also pushes the level at which isochronal ages are accurate (isochronal ages can have systematic errors of up to 25%, Torres et al. 2010).

3.4. Radial Velocity Analysis

We analyzed our radial velocity observations and archival observations taken from the literature to measure masses and orbital parameters for the WASP-47 planets. In our analysis, we combined our HARPS-N observations with previously published radial velocities from CORALIE (Hellier et al. 2012; Neveu-VanMalle et al. 2016), PFS (Dai et al. 2015), and HIRES (Sinukoff et al. 2017b). From our HARPS-N dataset, we excluded the four points we found to be contaminated

TABLE 1
HARPS-N RADIAL VELOCITIES OF WASP-47

BJD - 2454833	RV [m s ⁻¹]	σ_{RV} [m s ⁻¹]
2457226.561	-27014.60	6.43
2457226.699	-26987.90	4.84
2457226.721	-26982.21	6.71
2457227.561	-26937.25	2.63
2457227.713	-26954.63	2.55
2457228.566	-27113.16	4.71
2457228.700	-27142.69	4.98
2457229.562	-27219.22	5.11
2457229.703	-27190.29	3.24
2457230.572	-27039.26	2.59
2457230.711	-27010.20	2.34
2457254.520	-27210.88	3.77
2457256.548	-26932.08	2.20
2457256.641	-26933.99	3.06
2457257.644	-27101.64	3.34
2457267.487	-27151.78	2.43
2457267.602	-27127.38	2.23
2457268.521	-26968.72	7.43
2457268.624	-26945.85	2.77
2457269.542	-26995.84	2.31
2457270.526	-27188.86	1.85
2457271.530	-27172.97	1.88
2457272.568	-26967.95	2.45
2457273.544	-26970.22	2.09
2457301.412	-27017.29	1.95
2457301.521	-26992.78	2.21
2457302.411	-26931.79	2.08
2457302.524	-26936.49	2.99
2457324.337	-27134.85	3.00
2457325.323	-27192.62	3.33
2457325.417	-27190.58	2.67
2457330.315	-27046.38	2.67
2457330.443	-27031.60	2.93
2457331.316	-26930.42	2.97
2457331.421	-26929.30	2.55
2457333.328	-27202.65	2.60
2457336.316	-27018.83	2.47
2457336.398	-27036.13	2.99
2457557.701	-27149.24	2.56
2457558.695	-27093.68	2.09
2457559.702	-26902.75	2.53
2457560.684	-26931.92	3.67
2457562.695	-27116.92	3.47
2457563.687	-26918.20	4.10
2457565.691	-27101.52	3.66
2457566.698	-27143.80	2.79
2457573.722	-27054.63	3.49
2457574.613	-27167.37	2.72
2457574.701	-27157.09	2.51
2457576.584	-26880.69	3.16
2457576.685	-26886.91	2.42
2457579.695	-27041.15	7.68
2457580.680	-26877.83	7.44
2457616.560	-27138.59	6.88
2457617.581	-26939.47	1.98
2457618.579	-26882.95	2.53
2457651.460	-26875.57	2.16
2457652.459	-26982.58	2.18
2457653.463	-27155.02	2.81
2457654.464	-27057.53	2.88
2457655.492	-26870.08	5.08
2457658.510	-27083.94	4.73
2457659.516	-26895.47	2.20
2457661.490	-27123.19	2.53
2457669.458	-27063.11	2.80
2457670.456	-27140.53	3.07
2457671.451	-26981.35	1.97
2457672.454	-26870.44	1.88
2457721.368	-27000.32	2.36

TABLE 2
SUMMARY OF RADIAL VELOCITY OBSERVATIONS OF WASP-47

	HARPS-N	HIRES	PFS ^a	CORALIE
Number of usable observations	69	43	26	46
Standard deviation about best-fit	3.3 m s ⁻¹	3.7 m s ⁻¹	7.4 m s ⁻¹	13.5 m s ⁻¹
Mean photon-limited uncertainty	3.3 m s ⁻¹	2.0 m s ⁻¹	3.2 m s ⁻¹	12.1 m s ⁻¹
Time baseline	495 days	412 days	12 days	1622 days

NOTE. — *a*: In our final analysis, we exclude the PFS data. The standard deviation reported in the table is about the best-fit solution which did not include the PFS data. When the PFS data is included in the fit, its standard deviation about the best-fit model is 7.3 m s⁻¹.

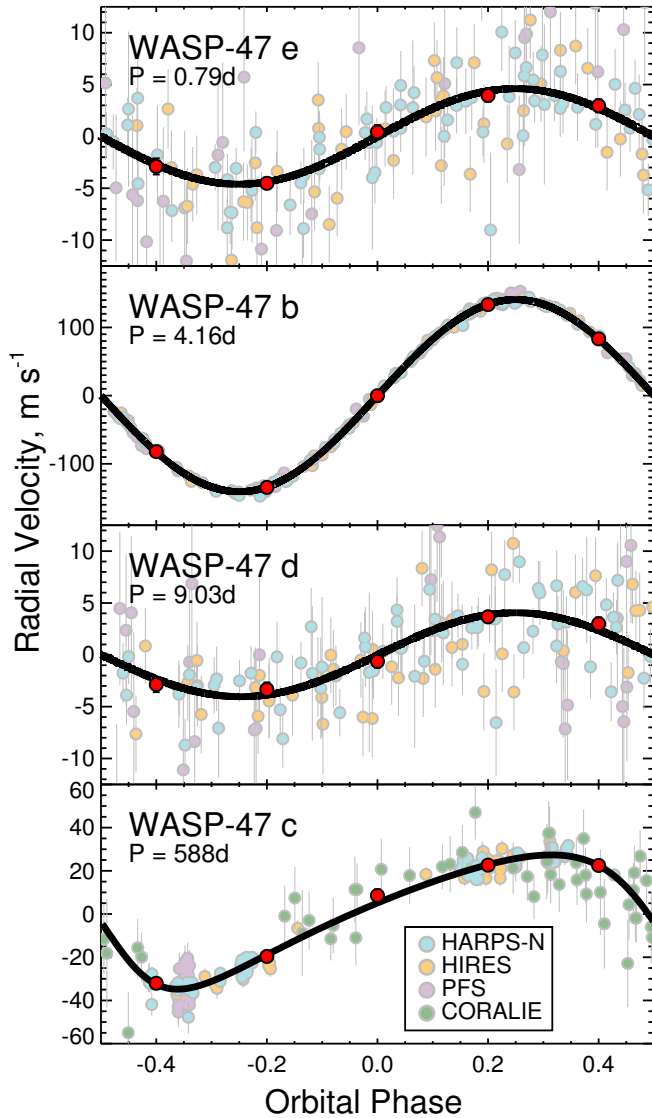


FIG. 1.— Radial velocity observations of WASP-47 from four spectrographs, folded on the periods of the four planets, with the best-fit model for each of the other three planets subtracted away. Data from HARPS-N are shown as pale blue dots, HIRES as pale orange dots, PFS as pale maroon dots, and CORALIE as pale green dots. The CORALIE data are only shown for WASP-47 c, as they are not of high enough precision to meaningfully constrain the orbits of WASP-47 e and WASP-47 d. The thick black lines are the best-fit models for each of the four planets, and the dark red dots are binned points. We note that we do not include the PFS velocities in our final analysis.

by sky background light and one point that was taken

during poor conditions and which exhibited a photon-limited velocity uncertainty of 16 m s⁻¹, six times greater than the typical uncertainty in our dataset. From the HIRES dataset, we excluded the points taken on the night of their Rossiter-McLaughlin observation (Sanchis-Ojeda et al. 2015; Sinukoff et al. 2017b). From all four RV datasets, we excluded points taken within two hours of the mid-transit time of WASP-47 b since those points are affected by the planet’s Rossiter-McLaughlin signal which we do not model³¹. The Rossiter-McLaughlin effects of the two other transiting planets are negligibly small so we retained points taken during their transits. We list our HARPS-N velocity observations in Table 1 and summarize the four datasets in Table 2.

We modeled the radial velocity of WASP-47 as a sum of four Keplerian functions, and do not attempt to model the gravitational interactions between the four planets. Even though mutual gravitational interactions do perturb the planets’ orbits (Becker et al. 2015; Almenara et al. 2016; Weiss et al. 2016a), the effect on the radial velocity curve is undetectably small (Dai et al. 2015; Sinukoff et al. 2017b). We confirmed this result holds over the longer time-span of our observations by numerically integrating the system. We used the same eccentricity priors for the RV analysis as we did for the transit analysis – specifically we forced the orbits of WASP-47 b and WASP-47 e to be circular, and we imposed a half-Gaussian prior on the eccentricity of WASP-47 d centered at 0 (without allowing negative eccentricity solutions) with a standard deviation of 0.014. For WASP-47 c, we allowed eccentricity and the argument of periastron to vary freely with only uniform priors imposed. For the three transiting planets, we imposed Gaussian priors on orbital period and time of transit at the values and uncertainties we derived in our transit analysis. We also imposed a prior that the RV semiamplitudes of all four planets be greater than zero, but the signals of all four planets were detected strongly enough that this prior had no effect.

WASP-47 is photometrically quiet, and we see no evidence in the radial velocities or activity indicators of correlations due to stellar activity, so we used a white noise model for our RV analysis, with separate instrumental “jitter” terms for data from the four different telescopes. We also fit for velocity zero-point offsets for the four different instruments. We did not impose any informative priors on the jitter terms and zero-point offsets. We explored parameter space using an MCMC algorithm with

³¹ This led to the exclusion of four HARPS-N data points and two HIRES datapoints.

affine invariant ensemble sampling, like for our transit analysis and our stellar parameter analysis. We used 100 walkers and evolved their positions for 150,000 steps each. To match the size of the chains from our transit analysis (Section 3.2) and our stellar parameter analysis (Section 3.3), we used the final 10,000 steps in our chains to estimate parameters. We confirmed the MCMC chains were converged by calculating the Gelman-Rubin statistics; the values were below 1.05 for all parameters.

We show the radial velocities from all four spectrographs and our best-fitting model in Figure 1. From our combined analysis with data from all four spectrographs, we measure masses that are more precise than, but consistent with previous determinations, except for the mass of WASP-47 e, which is somewhat at odds with the masses determined by Dai et al. (2015) and Sinukoff et al. (2017b). In particular, using data from all four spectrographs, we measure the mass of WASP-47 e to be $7.15 \pm 0.67 M_{\oplus}$, about $1.5\text{-}\sigma$ lower than both the measurements by Dai et al. (2015) of $12.2 \pm 3.7 M_{\oplus}$, and Sinukoff et al. (2017b) of $9.11 \pm 1.17 M_{\oplus}$.

We investigated the source of this discrepancy by repeating the RV fits with different datasets included and removed from the analysis. We found that the HARPS-N and HARPS-N datasets are quite consistent, both yielding masses for WASP-47 e between 6.5 and $7 M_{\oplus}$, but that the PFS dataset favors a planet mass almost a factor of two larger³². There are two possible explanations for the discrepancy between the PFS mass measurement and the HARPS-N/HIRES measurements.

1. The discrepancy is the result of random chance. The PFS measurement of WASP-47 e’s semi-amplitude is only $1.5\text{-}\sigma$ away from the HARPS-N/HIRES solution, a discrepancy that should happen in about 6.5% of all similar datasets. If this explanation is correct, then including the PFS data in our solution is appropriate and will help the mass measurement converge to the true mass.
2. The discrepancy is the result of some time-correlated systematic errors in the PFS velocities. In this case including the data in our solution is not appropriate and will not help our measurements converge to the true mass.

There are reasons to believe the PFS velocities of WASP-47 could be systematically erroneous – the scatter of the PFS data about the solution is 7.3 m s^{-1} , more than twice the photon-limited uncertainties listed by Dai et al. (2015), and considerably worse than both PFS’s typical RV precision (better than 2 m s^{-1} , Teske et al. 2016) and the radial velocity scatter from HARPS-N (3.3 m s^{-1}) and HIRES (3.7 m s^{-1}) in observations of WASP-47. Because the PFS observations were all taken over the course of only 12 days, if systematics are the cause of the large scatter in the velocities, any time correlations in the systematics would not necessarily average out.

Because of the risk of systematics contamination, and because the PFS data do not help much to constrain our

³² The discrepancy between our combined mass measurement and that of Sinukoff et al. (2017b) is mostly due to the fact that Sinukoff et al. (2017b) included the PFS data in their analysis, which pulled their solution to higher masses.

velocity solution (the dataset is both smaller and less precise than the HARPS-N and HIRES observations, and the time baseline is not as long as the CORALIE observations), we choose to exclude the PFS observations from our final analysis. We re-ran the same MCMC analysis as before using only data from CORALIE, HARPS-N, and HIRES, and determined new planet masses. The masses and uncertainties of WASP-47 b, c, and d were essentially unchanged, but the mass of WASP-47 e decreased by about $0.5\text{-}\sigma$ while the uncertainty was unchanged. The results of this RV analysis are reported in Table 3.

We measure masses of $6.83 \pm 0.66 M_{\oplus}$ for WASP-47 e, $363.1 \pm 7.3 M_{\oplus}$ for WASP-47 b, $13.1 \pm 1.5 M_{\oplus}$ for WASP-47 d, and a minimum mass of $M_p \sin i = 398.2 \pm 9.3 M_{\oplus}$ for WASP-47 c. WASP-47 c’s orbit is significantly eccentric, with $e_c = 0.296 \pm 0.017$. The longer time-baseline of the HARPS-N observations compared to the previously published HIRES dataset and the higher precision compared to the CORALIE dataset gives a more precise measurement of the outer planet’s orbital eccentricity and argument of periastron than before³³.

4. DYNAMICAL CONSTRAINTS

Unlike the three inner planets, which have precisely known (relative) orbital inclinations from their transit light curves, WASP-47 c has only been detected in radial velocity observations so far³⁴. In this section, we use dynamical arguments to constrain the inclination of WASP-47 c. We perform a variation of the analysis done by Becker & Adams (2017), who constrained WASP-47 c’s inclination by requiring that when perturbed by the outer planet, the three inner planets in the WASP-47 system all continually co-transit in the same orbital plane (where co-transit is defined as all of the planets crossing the star at any impact parameter, including grazing transits). Becker & Adams (2017) found that this requirement does not rule out orbits of WASP-47 c with high inclinations relative to the inner three planets, but that a realization of WASP-47 c with an inclination within a degree of the central projected plane of the star will always allow the inner three planets to transit.

Here we significantly strengthen the constraints placed by Becker & Adams (2017) by requiring that models of the WASP-47 system with WASP-47 c orbiting at various different inclinations reproduce other observed properties of the system. We relax the constraint that the planets all transit the star in the original orbital plane, and instead we require:

1. The inner planets around WASP-47 remain dynamically stable over integrations of 1 Myr.
2. The inner planets have mutual inclinations such that their transit impact parameters are as close

³³ We note that another possible explanation for WASP-47 c’s eccentricity is that it is caused by the un-modeled RV signal from an additional planet with half the orbital period of WASP-47 c (Anglada-Escudé et al. 2010), or the un-modeled signal from a longer-period planet (as postulated by Weiss et al. 2016a) contributing an RV acceleration. Our observations do not yet have the precision and time-baseline to distinguish these scenarios, so we interpret the signal as being caused by one eccentric planet.

³⁴ If WASP-47 c does happen to transit, it would not have been detected by K2 because it was at the wrong phase of its orbit during the 60 days of observations.

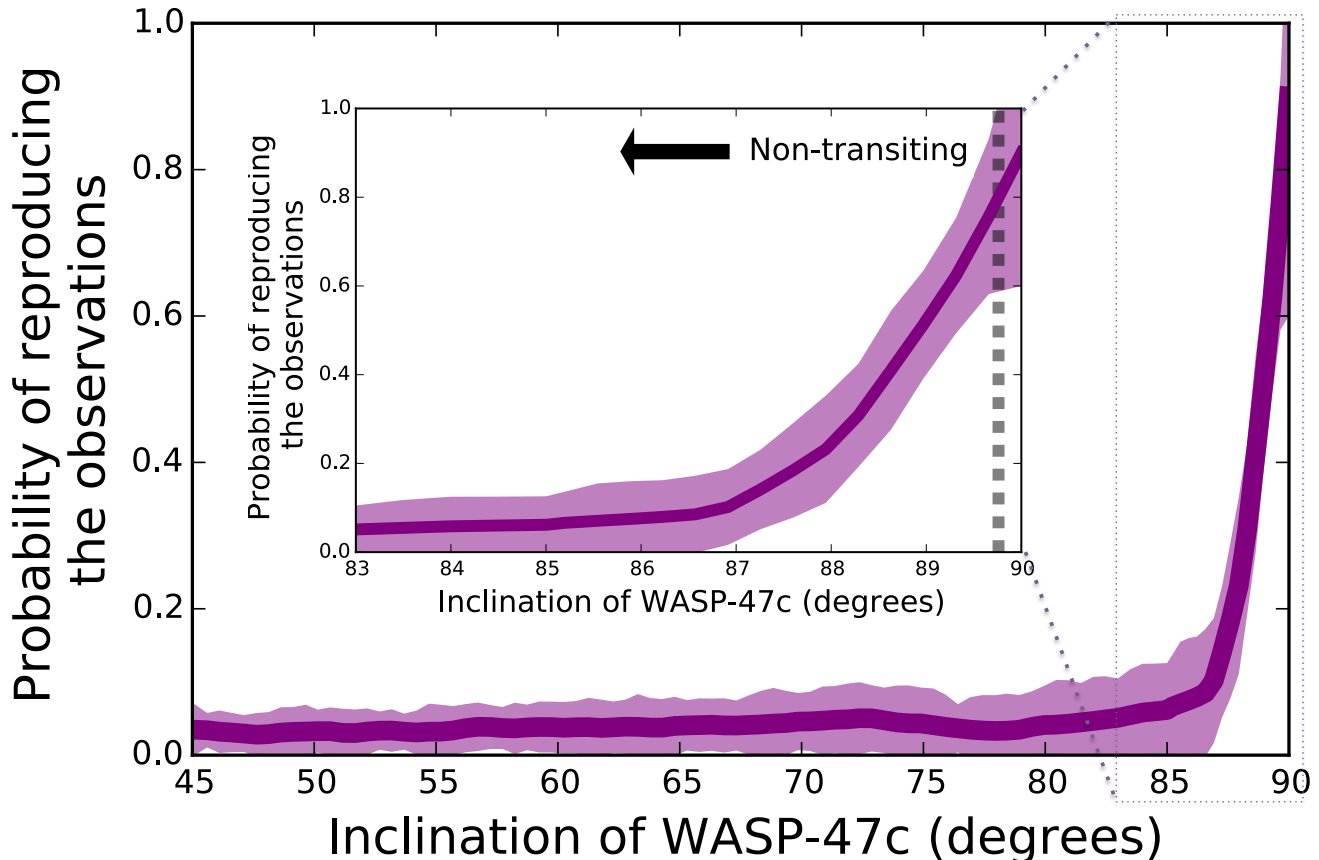


FIG. 2.— Constraints on the orbital inclination of WASP-47c. This plot shows the fraction of time the WASP-47 system can reproduce our observations as a function of the inclination of WASP-47c. The dark purple line is the average fraction of the time our simulations reproduce our observations of WASP-47, and the colored contours show the 1σ range calculated from the individual realizations. The inset diagram provides a zoomed-in version of the main figure to show the detail near $i_c = 90^\circ$ (i.e., near the orbital plane of the inner planets).

to zero as we measure (at 3σ confidence)³⁵.

3. WASP-47b has a sky-projected spin/orbit obliquity consistent with the result of Sanchis-Ojeda et al. (2015).

We conduct numerical N-body simulations using the Mercury6 (Chambers 1999) software package to evaluate the likelihood that WASP-47c allows these three criteria to be satisfied — that is, the likelihood that the simulations reproduce the observations at varying values of WASP-47c’s orbital inclination. In our simulations, we use a hybrid symplectic and Bulirsch-Stoer (B-S) integrator, requiring energy conservation to a part in 10^{-8} or better, and allowing each integration to run for 1 Myr with a starting time-step of 14 minutes. We run 2000 total 1 Myr integrations, each with randomly drawn initial conditions.

The choice of 1 Myr as an integration time was chosen for two reasons: first, the short time-step required for these simulations is computationally demanding and

³⁵ Here, although the fact that all three planets transit does not technically constrain their longitudes of ascending nodes, we assume the inner three planets are indeed coplanar. If the three planets did have high mutual inclinations, the probability that all three would transit is very small — a probability of about 1 in 1000 compared to a co-planar transit probability of roughly 1 in 15.

integrations of 1 Myr remain feasible; second, 1 Myr encapsulates many ($> 10^8$) dynamical times of the inner planet, and several (3-4) secular time scales. These timescales are important because orbital instabilities will occur on dynamical time scales, while motions in a single secular cycle will be expected to repeat in subsequent secular cycles. A integration time of 1 Myr allows us to effectively evaluate any dynamical instabilities, as well as encapsulate any long-term secular variations that may occur.

The initial conditions for each planet in each integration are drawn from the observations presented in Table 3. For most orbital parameters of the inner three planets, we draw from a normal distribution with mean and error as reported in the table. For orbital inclination, all measured inclinations are reported to be below 90 degrees, as the degeneracy between planets orbiting slightly above and slightly below the plane cannot be broken with photometric measurements. As such, we choose an inclination from within the range of measured errors, then assign this inclination to be above or below 90 degrees with equal probability. This process is repeated independently for each of the inner three planets in each integration.

The orbital parameters of the outer planet, WASP-47c, are also drawn from the observed values presented

in Table 3. To disentangle M_p and i , we choose a value for the inclination of WASP-47c for each integration, then choose a value of $M_p \sin i$ from the observed prior, and derive the planetary mass M_p .

Each integration results in one of two outcomes: (1) dynamical instabilities, in which planets collide with each other, collide with the central body, or are ejected from the system; or (2) dynamical stability. In this first case of dynamical instability, we assign a probability of those initial conditions reproducing the observations as being 0, as the system loses planets and/or changes orbits significantly. In the second, dynamically stable case, we can perform a second calculation using the results of the numerical simulations and determine the fraction of time that the set of initial conditions in a given integration reproduce the observations. The definition of reproducing the initial conditions requires the three criteria enumerated above.

Each integration results in a pairing of WASP-47c’s orbital inclination with a measure of the probability that that particular inclination (and other initial conditions) reproduces the observations. We calculate the average fraction of time within the trials in which observations are reproduced as a function of inclination by smoothing the measurements from individual integrations with a Savitzky-Golay filter (a standard low-pass filter; Savitzky & Golay 1964).

We show the results of our simulations in Figure 2. In particular, we show the smoothed function and the range of the fraction of time individual realizations of the system satisfy our observational criteria. Evidently, it is hard to reproduce the observed properties of the WASP-47 system if the outer planet is not aligned close to the inner planets’ orbital plane. Unlike the result of Becker & Adams (2017), even a perfectly edge-on system with an inclination of 90° does not guarantee that the inner three planets reproduce the observations, mainly because of the increased precision on measured planetary impact parameters.

Our constraints on the orbital inclination of WASP-47c also allow us to place approximate limits on the true mass of this planet by breaking the degeneracy in the measured $m \sin i$ between the planet’s mass and orbital inclination. We find that the 68% limit on the mass of WASP-47c is only 10% larger than the minimum mass, and that the true mass of WASP-47c is smaller than double the minimum mass with 93% confidence.

5. DISCUSSION

5.1. Constraints on the Composition of WASP-47e

Our new measurements and analyses have yielded the most precise planetary masses and radii yet for the WASP-47 planets, which give us the ability to make strong inferences about the planets’ compositions. We downloaded mass-radius relations for planets of various compositions³⁶ from Zeng et al. (2016), and compared the measured mass ($6.83 \pm 0.66 M_\oplus$) and radius ($1.810 \pm 0.027 R_\oplus$) of WASP-47e with these relations. We show a mass/radius diagram including the newly determined masses for WASP-47e and WASP-47d in Figure 3. Unlike most other small, highly irradiated planets (Dressing

et al. 2015), the mass and radius of WASP-47e are not consistent with an Earth-like composition (32.5% iron core, 67.5% silicate mantle) at the $p = 5 \times 10^{-4}$, or roughly $3.3\text{-}\sigma$ level³⁷. Instead, WASP-47e is less dense than an Earth-like rocky planet, and falls closer to the pure rock (MgSiO_3) mass/radius relation from Zeng et al. (2016).

There are several possibilities for what the composition of WASP-47e might be. One possibility is that WASP-47e is a rocky planet with a very small iron core mass fraction compared to the Earth. Assuming a two-component iron core/rocky silicate mantle model, in this case, we would infer an iron fraction of $1.4\% \pm 8.4\%$. We believe this scenario is unlikely. Theoretically, given the small scatter in chemical abundances of stars in the Solar neighborhood, rocky planet radii should not change much more than 2% due to differences in compositions (Grasset et al. 2009), while WASP-47e’s radius is 7% larger than an Earth-like planet with the same mass. Moreover, observations of small, likely rocky planets near their host stars have shown that rocky exoplanets tend to have compositions consistent with that of the Earth (Dressing et al. 2015; Buchhave et al. 2016). It is unclear how a planet of this size, around a star of such high metallicity/iron content, could avoid accumulating any substantial amount of iron.

Instead, a more likely possibility is that WASP-47e has an Earth-like core and mantle that is surrounded by a volatile-rich envelope. This type of interior structure is believed to be common among super-Earths and sub-Neptunes discovered by *Kepler* and K2 since RV observations have shown that most of these planets larger than about $1.6 R_\oplus$ have densities too low to be explained by rocky compositions (Marcy et al. 2014; Weiss & Marcy 2014; Rogers 2015; Dressing et al. 2015; Sinukoff et al. 2017a). Due to its short (19 hour) orbital period, WASP-47e is so highly irradiated that any hydrogen/helium envelope would quickly be lost via photo-evaporation (Penz et al. 2008; Sanz-Forcada et al. 2011; Lopez et al. 2012), so any envelope around WASP-47e must be made of water or some other high-metallicity volatile material (Lopez 2016). Using the model described by Lopez (2016), we find that an Earth-like core and mantle surrounded by a water (or in this case, steam) layer making up 17% of the WASP-47e’s total mass is consistent with our observations.

WASP-47e joins 55 Cnc e as the only ultra-short period (USP, $P < 1$ day) planets with densities too low to be consistent with an Earth-like composition³⁸ (Sanchis-Ojeda et al. 2014). Mass measurements of other transiting USP planets from *Kepler* and CoRoT have all been consistent with Earth-like compositions (*Kepler*-10 b, Batalha et al. 2011; Dumusque et al. 2014; Weiss et al. 2016b; *Kepler*-78 b, Howard et al. 2013; Pepe et al. 2013; Grunblatt et al. 2015; CoRoT-7 b, Queloz et al. 2009;

³⁷ If we instead assume the slightly larger mass from our RV analysis including the PFS data, this conclusion still holds. Assuming a two-component iron core/rocky silicate mantle model, the median iron fraction for WASP-47e would be $4.3\% \pm 9.8\%$. An Earth-like 32.5% iron core fraction is excluded at the $p = 1.5 \times 10^{-3}$ or $3\text{-}\sigma$ level.

³⁸ KOI 1843.03 must have a high density to avoid tidal disruption and therefore a larger iron core mass fraction than Earth (Rappaport et al. 2013).

³⁶ The mass/radius relations are available at <https://www.cfa.harvard.edu/~lzeng/tables/mrtable3.txt>

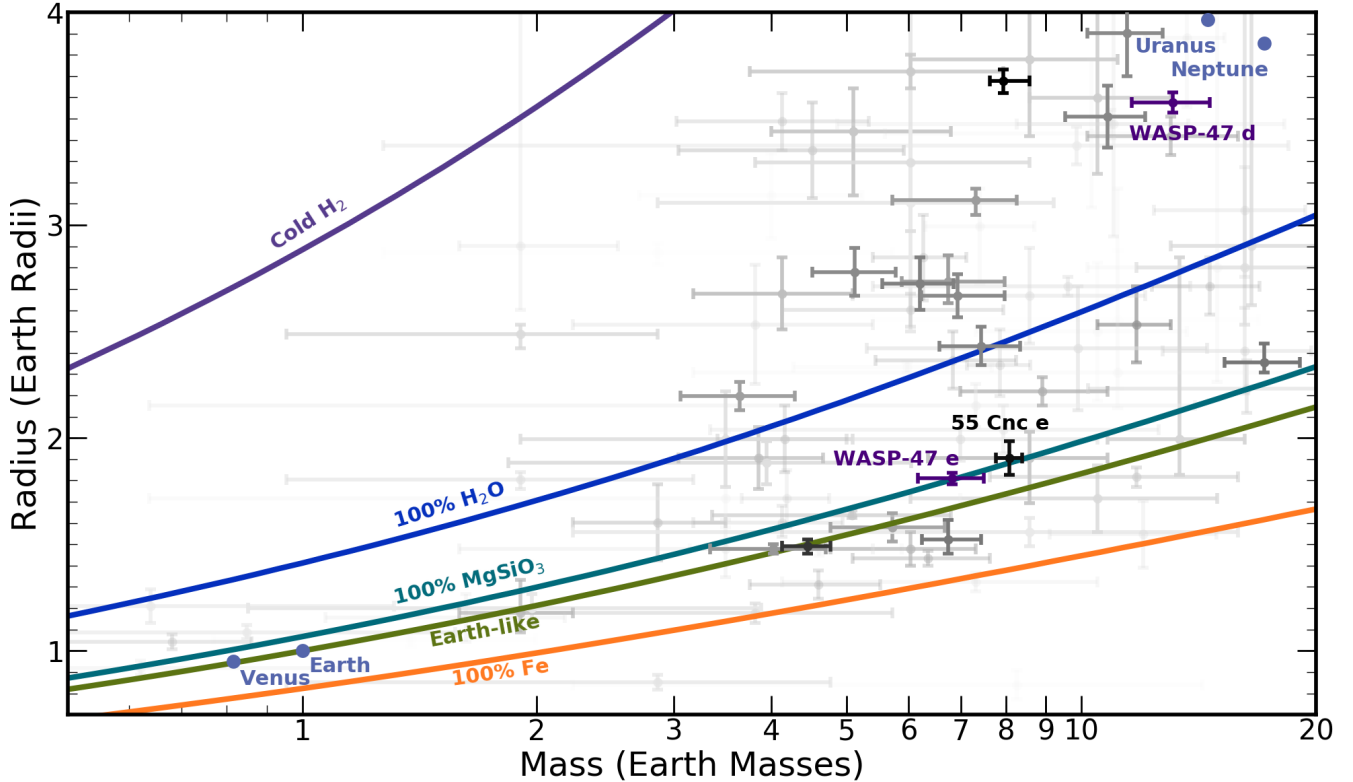


FIG. 3.— The mass/radius diagram for small exoplanets. Planet masses and radii are taken from the NASA Exoplanet Archive (Akeson et al. 2013), accessed 2017 Feb 22. The symbol darkness is proportional to the precision with which the masses and radii are determined. Overplotted are theoretical mass/radius relations for solid planets of different compositions from Zeng et al. (2016) and for cold hydrogen planets from Seager et al. (2007). Solar system planets are shown in blue, and the WASP-47 planets are shown in purple. We also label 55 Cnc e to show the similarity in composition between it and WASP-47 e— both of these planets are less dense than an Earth-like composition, and likely have some volatiles around an Earth-like core.

Haywood et al. 2014; K2-106 b, Sinukoff et al. 2017a; Guenther et al. 2017; and HD 3167 b, Christiansen et al. 2017; Gandolfi et al. 2017).

Of all the USP planets with measured masses, WASP-47 e and 55 Cnc e are the two largest and most massive, so perhaps the largest USP planets preferentially retain some volatile materials. However, WASP-47 e and 55 Cnc e are also the two USP planets with the most precise mass determinations — it is possible that some of the other lower-mass USP planets also have densities too low to be explained by Earth-like compositions, and our data are not yet constraining enough to tell.

How might WASP-47 e and 55 Cnc e have come to possess such compositions? Previously it has been thought that USP planets might commonly be the remains of puffy planets (but probably not hot Jupiters, Winn et al. 2017) after photo-evaporation stripped them of most or all of their volatile envelopes. Evidence for this includes the fact that almost all USP planets or candidates have radii smaller than about twice that of the Earth (Jackson et al. 2013; Sanchis-Ojeda et al. 2014; Lopez 2016), in contrast to the large population of less irradiated planets with radii between 2 and 4 R_{\oplus} at longer orbital periods (Fressin et al. 2013; Petigura et al. 2013b). WASP-47 e and 55 Cnc e might therefore be the remnants of larger planets that were massive enough to accrete a significant amount of both hydrogen and denser volatile materials before the hydrogen was subsequently lost to photoevaporation. On the other hand, WASP-47 e and 55

Cnc e may be unusual – in addition to being the only known USPs inconsistent with Earth-like interior structures, these planets are also the only well characterized USPs in systems with multiple Jovian planets. If this is not a coincidence and these planets are not typical of USPs, then a more exotic origin scenario may be required. One such possibility is that these planets are the remnant cores of hot Jupiters stripped by Roche lobe overflow (Valsecchi et al. 2014; Jackson et al. 2017). Although this mechanism cannot explain the general population of rocky USPs, this could explain WASP-47 e and 55 Cnc e’s unusually low densities for such highly irradiated planets, their similar orbital periods (determined by the orbital radius at which Roche lobe overflow began), and the fact that these two objects were found in systems with multiple giant planets.

Finally, we note several additional similarities between the WASP-47 system and the 55 Cnc system. Both host stars have high metallicity ($[\text{Fe}/\text{H}] = 0.38$ for WASP-47, and $[\text{Fe}/\text{H}] = 0.31$ for 55 Cnc, Valenti & Fischer 2005), both systems have ultra-short-period planets which likely have a layer of dense volatile materials (WASP-47 e and 55 Cnc e), both systems have short-period giant planets (WASP-47 b and the 15d period warm Jupiter 55 Cnc b), and both systems have long-period giant planets (WASP-47 c and the 5000d period 55 Cnc d). While the 55 Cnc planets may not be as closely aligned with one another as the WASP-47 planets (only the innermost planet around 55 Cnc is known to transit, and astrometric measure-

ments have shown a misalignment for the giant outer planet 55 Cnc d (McArthur et al. 2004), the similarities between these two system architectures suggest similar origins.

5.2. Constraints on the Composition of WASP-47 d

We also determine a precise mass and radius for WASP-47 d of $13.1 \pm 1.5 M_{\oplus}$ and $3.576 \pm 0.046 R_{\oplus}$ respectively. On a mass/radius diagram (Figure 3), WASP-47 d is close to, but slightly smaller and less massive than the two Solar system ice giants, Uranus and Neptune. Like Uranus and Neptune, WASP-47 d must have a low density hydrogen/helium envelope to match our mass and radius measurements, but most of the mass of the planet’s mass is in a dense core. Using the models from Lopez & Fortney (2014), we find that if the interior has an Earth-like composition with an iron core and rocky mantle, the hydrogen/helium envelope around WASP-47 d would have a mass fraction of about 5%. If instead, the solid core is rich in water or other high metallicity volatiles, the hydrogen/helium envelope mass fraction would be closer to 2%.

5.3. Orbital Inclination of WASP-47 c

Even though WASP-47 c has only been detected in radial velocities, in Section 4, we were able to put strong constraints on its orbital inclination by requiring dynamical perturbations from its orbit not disrupt the well aligned, co-transiting state of the inner three planets. We found that WASP-47 d likely has an inclination within a few degrees of an edge-on 90° orbit.

The fact that WASP-47 c likely orbits in the same plane as the three transiting planets suggests that the system formed in a dynamically quiet manner. If the hot Jupiter, WASP-47 b, formed beyond the snow-line and migrated after being scattered by WASP-47 c, we might expect the plane of WASP-47 c’s orbit to be different from the plane of the inner system. Instead, we see a picture more consistent with formation and migration that largely happened in the plane of the protoplanetary disk. In particular, the fact that WASP-47 e likely has a layer of dense volatile material like water suggests that it may have formed beyond the snow-line and migrated to its current location through the protoplanetary disk. WASP-47 c’s relatively high eccentricity is somewhat difficult to explain in this context, because any eccentricity would have been damped by the disk. In this scenario, the eccentricity must have been excited after the disk dissipated, possibly by another, more distant planet, as suggested by Weiss et al. (2016a).

5.4. WASP-47 c’s Transit Probability

Another, more practical, implication of the likely close alignment of WASP-47 c with the inner transiting system is that the probability of WASP-47 c transiting is greatly enhanced compared to the naive geometric transit probability. The expression for geometric transit probability is given by Sackett (1999):

$$P_{\text{transit,geom}} = \frac{\int_{i_t}^{90^\circ} \sin i \, di}{\int_{0^\circ}^{90^\circ} \sin i \, di} \quad (1)$$

where i is the planet’s inclination, and i_t is the inclination above which the planet will transit, which depends on the

orbital eccentricity e , argument of periastron ω_p , semi-major axis a , stellar radius R_* , and planetary radius R_p as follows:

$$\cos i_t = \frac{R_p + R_*}{a} \times \frac{1 + e \sin \omega_p}{1 - e^2} \quad (2)$$

We generalized the geometric expression by including a function $\mathcal{P}(i)$, the fraction of time our simulated systems reproduced observations of WASP-47 inside the integrals, giving:

$$P_{\text{transit,mod}} = \frac{\int_{i_t}^{90^\circ} \mathcal{P}(i) \sin i \, di}{\int_{0^\circ}^{90^\circ} \mathcal{P}(i) \sin i \, di} \quad (3)$$

Here, for $\mathcal{P}(i)$ we use the Savitzky-Golay filtered fraction of times that our numerical simulations reproduced observations of WASP-47, and for i_t we use 89.66° .

Without *a priori* knowledge of our inclination constraints for WASP-47 c, the transit probability is about 0.6%. When we take into account our dynamical inclination constraints, the probability increases by more than an order of magnitude to about 10% – the same *a priori* transit probability of a typical hot Jupiter.

If WASP-47 c is found to transit, it would open the door to future sophisticated investigations into the properties and formation history of the WASP-47 planets. It would be possible to study the atmosphere of both WASP-47 b and WASP-47 c in transit with the upcoming *James Webb Space Telescope*, determine and compare atmospheric abundances, and infer these planets’ birthplaces (Öberg et al. 2011). A detection of a transit of WASP-47 c could make the WASP-47 system a key to unlocking the origin of hot Jupiters.

Detecting a transit of WASP-47 c should not be difficult - the transit depth would likely be about 1%, easily attainable by ground-based telescopes with moderate apertures. The transit duration will be long - an equatorial transit of WASP-47 c would last 14 hours, so a successful detection would likely require a coordinated ground-based campaign with several telescopes longitudinally dispersed around the globe. At present, the largest obstacle to successfully recovering a transit of WASP-47 c is the uncertainty in the transit time. The last transit window happened around 9 January 2017, while WASP-47 was unobservable behind the Sun, with an uncertainty in transit time of 4.8 days. The next several transit windows will be around 21 August 2018 \pm 6.5 days, 31 March 2020 \pm 8.6 days, and 10 November 2021 \pm 10.8 days. It would take a massive ground-based campaign to cover enough of these transit windows to ensure success. Although the uncertainties on the transit times are large now, they will sharpen considerably once precise RV spectrographs have completed observing a full orbital period of WASP-47 c. We will continue to observe WASP-47 with HARPS-N in the coming years to refine the orbital period and ephemeris of WASP-47 c in preparation for the chance to detect the planet in transit.

6. SUMMARY

We have investigated the WASP-47 planetary system, which is known to host a hot Jupiter, two smaller transiting planets flanking the hot Jupiter, and a long-period Jovian companion. Using new data from the HARPS-N

spectrograph and previously published data from the K2 mission and other ground-based spectrographs, we have measured the masses and radii of the transiting planets, and determined the orbit of the outer planet. Our main conclusions are summarized as follows:

1. We have measured the most precise masses and radii for the WASP-47 planets yet. The innermost planet, WASP-47 e, has a mass of $6.83 \pm 0.66 M_{\oplus}$ and a radius $1.810 \pm 0.027 R_{\oplus}$. The hot Jupiter, WASP-47 b has mass $363.1 \pm 7.3 M_{\oplus}$ and a radius $12.63 \pm 0.15 R_{\oplus}$. We find the Neptune-sized planet, WASP-47 d, has a mass $13.1 \pm 1.5 M_{\oplus}$ and radius $3.576 \pm 0.046 R_{\oplus}$. The outer Jovian planet, WASP-47 c is not known to transit, so from our radial velocity observations, we only measure the planet’s minimum mass $m \sin i$ of $398.2 \pm 9.3 M_{\oplus}$.
2. WASP-47 e, unlike most other planets in ultra short period orbits, does not have an Earth-like composition. We find that WASP-47 e is not dense enough to have an iron core with the same mass fraction as terrestrial planets in the Solar system. Instead, WASP-47 e likely has a volatile rich (possibly water/steam) envelope comprising 17% its total mass on top of an Earth-like core.
3. We show using dynamical simulations that the inclination of WASP-47 c is likely well aligned with the inner transiting system. The orbital inclination of WASP-47 c is likely within a few degrees of edge on in order to not disrupt the inner transiting planets from their present-day well aligned configuration. This alignment, plus the alignment between the planets’ orbits and the stellar spin axis (Sanchis-Ojeda et al. 2015) suggests a dynamically quiet formation/migration scenario for the WASP-47 planets that kept all of the planets in the plane of the protoplanetary disk. The outer planet is much more likely to transit than the geometric transit probability, motivating campaigns to observe the transit in future opportunities. Additionally, this limit on the inclination suggests that the true mass of the WASP-47 c is likely close to the measured $M_P \sin i$.

Future radial velocity observations of WASP-47 will both continue to improve the precision on the masses of the two smaller planets, and will greatly improve the precision on the predicted transit time of WASP-47 c. Sharpening the transit predictions will be hugely important to making a campaign to detect or rule out transits of WASP-47 c feasible.

We thank Jason Eastman, Jonathan Irwin, Laura Kreidberg, Willie Torres, Lauren Weiss, and George Zhou for helpful conversations. We thank Josh Winn for helpful

comments on the manuscript and the anonymous referee for a thoughtful report. A.V. and J.C.B are supported by the NSF Graduate Research Fellowship, grant nos. DGE 1144152 and DGE 1256260, respectively. This work was performed in part under contract with the California Institute of Technology/Jet Propulsion Laboratory funded by NASA through the Sagan Fellowship Program executed by the NASA Exoplanet Science Institute. D.W.L. acknowledges partial support from the TESS mission through a sub-award from the Massachusetts Institute of Technology to the Smithsonian Astrophysical Observatory. The research leading to these results has received funding from the European Union Seventh Framework Programme (FP7/2007-2013) under Grant Agreement n. 313014 (ETA-EARTH). Parts of this work have been supported by NASA under grants No. NNX15AC90G and NNX17AB59G issued through the Exoplanets Research Program. This publication was made possible through the support of a grant from the John Templeton Foundation. The opinions expressed in this publication are those of the authors and do not necessarily reflect the views of the John Templeton Foundation.

This work is based on observations made with the Italian Telescopio Nazionale Galileo (TNG) operated on the island of La Palma by the Fundacin Galileo Galilei of the INAF (Istituto Nazionale di Astrofisica) at the Spanish Observatorio del Roque de los Muchachos of the Instituto de Astrofisica de Canarias. The HARPS-N project was funded by the Prodex Program of the Swiss Space Office (SSO), the Harvard University Origin of Life Initiative (HUOLI), the Scottish Universities Physics Alliance (SUPA), the University of Geneva, the Smithsonian Astrophysical Observatory (SAO), and the Italian National Astrophysical Institute (INAF), University of St. Andrews, Queens University Belfast and University of Edinburgh. This work was supported in part by the NASA Exoplanets Research Program.

This work used the Extreme Science and Engineering Discovery Environment (XSEDE), which is supported by National Science Foundation grant number ACI-1053575. This research was done using resources provided by the Open Science Grid, which is supported by the National Science Foundation and the U.S. Department of Energy’s Office of Science. We have made use of NASA’s Astrophysics Data System and the NASA Exoplanet Archive, which is operated by the California Institute of Technology, under contract with the National Aeronautics and Space Administration under the Exoplanet Exploration Program.

This paper includes data collected by the *Kepler*/K2 mission. Funding for the *Kepler* mission is provided by the NASA Science Mission directorate. Some of the data presented in this paper were obtained from the Mikulski Archive for Space Telescopes (MAST). STScI is operated by the Association of Universities for Research in Astronomy, Inc., under NASA contract NAS5-26555. Support for MAST for non-HST data is provided by the NASA Office of Space Science via grant NNX13AC07G and by other grants and contracts.

Facilities: Kepler/K2, TNG (HARPS-N)

REFERENCES

- Almenara, J. M., Díaz, R. F., Bonfils, X., & Udry, S. 2016, *A&A*, 595, L5
- Anglada-Escudé, G., López-Morales, M., & Chambers, J. E. 2010, *ApJ*, 709, 168
- Baranne, A., Queloz, D., Mayor, M., et al. 1996, *A&AS*, 119, 373
- Batalha, N. M., Borucki, W. J., Bryson, S. T., et al. 2011, *ApJ*, 729, 27
- Batygin, K., Bodenheimer, P. H., & Laughlin, G. P. 2016, *ApJ*, 829, 114
- Becker, J. C., & Adams, F. C. 2017, *MNRAS*, 468, 549
- Becker, J. C., Vanderburg, A., Adams, F. C., Rappaport, S. A., & Schwengel, H. M. 2015, *ApJ*, 812, L18
- Bonomo, A. S., Sozzetti, A., Lovis, C., et al. 2014, *A&A*, 572, A2
- Brewer, J. M., Fischer, D. A., Basu, S., Valenti, J. A., & Piskunov, N. 2015, *ApJ*, 805, 126
- Brewer, J. M., Fischer, D. A., Valenti, J. A., & Piskunov, N. 2016, *ApJS*, 225, 32
- Buchhave, L. A., Latham, D. W., Johansen, A., et al. 2012, *Nature*, 486, 375
- Buchhave, L. A., Bizzarro, M., Latham, D. W., et al. 2014, *Nature*, 509, 593
- Buchhave, L. A., Dressing, C. D., Dumusque, X., et al. 2016, *AJ*, 152, 160
- Burke, C. J., Christiansen, J. L., Mullally, F., et al. 2015, *ApJ*, 809, 8
- Chambers, J. E. 1999, *MNRAS*, 304, 793
- Christiansen, J. L., Vanderburg, A., Burt, J., et al. 2017, *ArXiv e-prints*, arXiv:1706.01892
- Claret, A., & Bloemen, S. 2011, *A&A*, 529, A75
- Collins, K. A., Kielkopf, J. F., & Stassun, K. G. 2017, *AJ*, 153, 78
- Cosentino, R., Lovis, C., Pepe, F., et al. 2012, in *Society of Photo-Optical Instrumentation Engineers (SPIE) Conference Series*, Vol. 8446, *Society of Photo-Optical Instrumentation Engineers (SPIE) Conference Series*
- Crossfield, I. J. M., Petigura, E., Schlieder, J. E., et al. 2015, *ApJ*, 804, 10
- Crossfield, I. J. M., Ciardi, D. R., Isaacson, H., et al. 2017, *ArXiv e-prints*, arXiv:1701.03811
- Dai, F., Winn, J. N., Arriagada, P., et al. 2015, *ApJ*, 813, L9
- David, T. J., Hillenbrand, L. A., Petigura, E. A., et al. 2016, *Nature*, 534, 658
- Dotter, A., Chaboyer, B., Jevremović, D., et al. 2008, *ApJS*, 178, 89
- Dressing, C. D., & Charbonneau, D. 2013, *ApJ*, 767, 95
- Dressing, C. D., Newton, E. R., Schlieder, J. E., et al. 2017a, *ApJ*, 836, 167
- Dressing, C. D., Charbonneau, D., Dumusque, X., et al. 2015, *ApJ*, 800, 135
- Dressing, C. D., Vanderburg, A., Schlieder, J. E., et al. 2017b, *ArXiv e-prints*, arXiv:1703.07416
- Dumusque, X., Bonomo, A. S., Haywood, R. D., et al. 2014, *ApJ*, 789, 154
- Eastman, J., Gaudi, B. S., & Agol, E. 2013, *PASP*, 125, 83
- Fressin, F., Torres, G., Charbonneau, D., et al. 2013, *ApJ*, 766, 81
- Gandolfi, D., Barragán, O., Hatzes, A. P., et al. 2017, *ArXiv e-prints*, arXiv:1706.02532
- Goldreich, P., & Soter, S. 1966, *Icarus*, 5, 375
- Goodman, J., & Weare, J. 2010, *Communications in Applied Mathematics and Computational Science*, 5, 65
- Grasset, O., Schneider, J., & Sotin, C. 2009, *ApJ*, 693, 722
- Grunblatt, S. K., Howard, A. W., & Haywood, R. D. 2015, *ApJ*, 808, 127
- Guenther, E. W., Barragan, O., Dai, F., et al. 2017, *ArXiv e-prints*, arXiv:1705.04163
- Haywood, R. D., Collier Cameron, A., Queloz, D., et al. 2014, *MNRAS*, 443, 2517
- Hellier, C., Anderson, D. R., Collier Cameron, A., et al. 2012, *MNRAS*, 426, 739
- Holman, M. J., & Murray, N. W. 2005, *Science*, 307, 1288
- Holman, M. J., Fabrycky, D. C., Ragozzine, D., et al. 2010, *Science*, 330, 51
- Howard, A. W., Sanchis-Ojeda, R., Marcy, G. W., et al. 2013, *Nature*, 503, 381
- Howell, S. B., Sobeck, C., Haas, M., et al. 2014, *PASP*, 126, 398
- Huang, C., Wu, Y., & Triaud, A. H. M. J. 2016, *ApJ*, 825, 98
- Jackson, B., Arras, P., Penev, K., Peacock, S., & Marchant, P. 2017, *ApJ*, 835, 145
- Jackson, B., Stark, C. C., Adams, E. R., Chambers, J., & Deming, D. 2013, *ApJ*, 779, 165
- Kipping, D. M. 2013, *MNRAS*, 435, 2152
- Kurucz, R. L. 1992, in *IAU Symposium*, Vol. 149, *The Stellar Populations of Galaxies*, ed. B. Barbuy & A. Renzini, 225
- Libralato, M., Nardiello, D., Bedin, L. R., et al. 2016, *MNRAS*, 463, 1780
- Lissauer, J. J., Fabrycky, D. C., Ford, E. B., et al. 2011, *Nature*, 470, 53
- Lopez, E. D. 2016, *ArXiv e-prints*, arXiv:1610.01170
- Lopez, E. D., & Fortney, J. J. 2014, *ApJ*, 792, 1
- Lopez, E. D., Fortney, J. J., & Miller, N. 2012, *ApJ*, 761, 59
- Malavolta, L., Borsato, L., Granata, V., et al. 2017, *ArXiv e-prints*, arXiv:1703.06885
- Mandel, K., & Agol, E. 2002, *ApJ*, 580, L171
- Mann, A. W., Newton, E. R., Rizzuto, A. C., et al. 2016a, *AJ*, 152, 61
- Mann, A. W., Gaidos, E., Mace, G. N., et al. 2016b, *ApJ*, 818, 46
- Mann, A. W., Gaidos, E., Vanderburg, A., et al. 2017, *AJ*, 153, 64
- Marcy, G. W., Isaacson, H., Howard, A. W., et al. 2014, *ApJS*, 210, 20
- Martinez, A. O., Crossfield, I. J. M., Schlieder, J. E., et al. 2017, *ApJ*, 837, 72
- McArthur, B. E., Endl, M., Cochran, W. D., et al. 2004, *ApJ*, 614, L81
- Miller-Ricci, E., Rowe, J. F., Sasselov, D., et al. 2008, *ApJ*, 682, 586
- Mortier, A., Santos, N. C., Sousa, S. G., et al. 2013, *A&A*, 558, A106
- Mortier, A., Sousa, S. G., Adibekyan, V. Z., Brandão, I. M., & Santos, N. C. 2014, *A&A*, 572, A95
- Muirhead, P. S., Johnson, J. A., Apps, K., et al. 2012, *ApJ*, 747, 144
- Neveu-VanMalle, M., Queloz, D., Anderson, D. R., et al. 2016, *A&A*, 586, A93
- Öberg, K. I., Murray-Clay, R., & Bergin, E. A. 2011, *ApJ*, 743, L16
- Obermeier, C., Henning, T., Schlieder, J. E., et al. 2016, *AJ*, 152, 223
- Penz, T., Micela, G., & Lammer, H. 2008, *A&A*, 477, 309
- Pepe, F., Mayor, M., Galland, F., et al. 2002, *A&A*, 388, 632
- Pepe, F., Cameron, A. C., Latham, D. W., et al. 2013, *Nature*, 503, 377
- Petigura, E. A., Howard, A. W., & Marcy, G. W. 2013a, *Proceedings of the National Academy of Science*, 110, 19273
- Petigura, E. A., Marcy, G. W., & Howard, A. W. 2013b, *ApJ*, 770, 69
- Petigura, E. A., Schlieder, J. E., Crossfield, I. J. M., et al. 2015, *ApJ*, 811, 102
- Queloz, D., Bouchy, F., Moutou, C., et al. 2009, *A&A*, 506, 303
- Rappaport, S., Sanchis-Ojeda, R., Rogers, L. A., Levine, A., & Winn, J. N. 2013, *ApJ*, 773, L15
- Rappaport, S., Levine, A., Chiang, E., et al. 2012, *ApJ*, 752, 1
- Rodriguez, J. E., Zhou, G., Vanderburg, A., et al. 2017, *ArXiv e-prints*, arXiv:1701.03807
- Rogers, L. A. 2015, *ApJ*, 801, 41
- Sackett, P. D. 1999, in *NATO Advanced Science Institutes (ASI) Series C*, Vol. 532, *NATO Advanced Science Institutes (ASI) Series C*, ed. J.-M. Mariotti & D. Alloin, 189
- Sanchis-Ojeda, R., Rappaport, S., Winn, J. N., et al. 2014, *ApJ*, 787, 47
- Sanchis-Ojeda, R., Winn, J. N., Dai, F., et al. 2015, *ApJ*, 812, L11
- Santos, N. C., Sousa, S. G., Mortier, A., et al. 2013, *A&A*, 556, A150
- Sanz-Forcada, J., Micela, G., Ribas, I., et al. 2011, *A&A*, 532, A6
- Savitzky, A., & Golay, M. J. E. 1964, *Analytical Chemistry*, 36, 1627
- Seager, S., Kuchner, M., Hier-Majumder, C. A., & Militzer, B. 2007, *ApJ*, 669, 1279
- Sinukoff, E., Howard, A. W., Petigura, E. A., et al. 2016, *ApJ*, 827, 78
- . 2017a, *AJ*, 153, 271
- . 2017b, *AJ*, 153, 70
- Snedden, C. 1973, *ApJ*, 184, 839

- Sousa, S. G. 2014, ARES + MOOG: A Practical Overview of an Equivalent Width (EW) Method to Derive Stellar Parameters, ed. E. Niemczura, B. Smalley, & W. Pych, 297–310
- Sousa, S. G., Santos, N. C., Adibekyan, V., Delgado-Mena, E., & Israelian, G. 2015, *A&A*, 577, A67
- Sozzetti, A., Torres, G., Charbonneau, D., et al. 2007, *ApJ*, 664, 1190
- Steffen, J. H., & Agol, E. 2005, *MNRAS*, 364, L96
- Steffen, J. H., Ragozzine, D., Fabrycky, D. C., et al. 2012, *Proceedings of the National Academy of Science*, 109, 7982
- Teske, J. K., Shectman, S. A., Vogt, S. S., et al. 2016, *AJ*, 152, 167
- Torres, G., Andersen, J., & Giménez, A. 2010, *A&A Rev.*, 18, 67
- Valenti, J. A., & Fischer, D. A. 2005, *ApJS*, 159, 141
- Valsecchi, F., Rasio, F. A., & Steffen, J. H. 2014, *ApJ*, 793, L3
- Vanderburg, A., & Johnson, J. A. 2014, *PASP*, 126, 948
- Vanderburg, A., Montet, B. T., Johnson, J. A., et al. 2015, *ApJ*, 800, 59
- Vanderburg, A., Becker, J. C., Kristiansen, M. H., et al. 2016a, *ApJ*, 827, L10
- Vanderburg, A., Latham, D. W., Buchhave, L. A., et al. 2016b, *ApJS*, 222, 14
- Weiss, L. M., & Marcy, G. W. 2014, *ApJ*, 783, L6
- Weiss, L. M., Deck, K., Sinukoff, E., et al. 2016a, *ArXiv e-prints*, arXiv:1612.04856
- Weiss, L. M., Rogers, L. A., Isaacson, H. T., et al. 2016b, *ApJ*, 819, 83
- Winn, J. N., Sanchis-Ojeda, R., Rogers, L., et al. 2017, *ArXiv e-prints*, arXiv:1704.00203
- Yi, S., Demarque, P., Kim, Y.-C., et al. 2001, *ApJS*, 136, 417
- Zeng, L., Sasselov, D. D., & Jacobsen, S. B. 2016, *ApJ*, 819, 127

TABLE 3
 SYSTEM PARAMETERS FOR WASP-47

Parameter	Value		68.3% Confidence Interval Width	Comment
<i>Stellar Parameters</i>				
Right Ascension	22:04:48.7			
Declination	-12:01:08			
$M_\star [M_\odot]$	1.040	±	0.031	A,B
$R_\star [R_\odot]$	1.137	±	0.013	A,B
Limb darkening q_1	0.396	±	0.018	B
Limb darkening q_2	0.423	±	0.017	B
Stellar Density $\rho_\star [g\ cm^{-3}]$	0.999	±	0.014	B
$\log g_\star$ [cgs]	4.3437	±	0.0063	A,B,C
[M/H]	0.38	±	0.05	C
T_{eff} [K]	5552	±	75	C
<i>WASP-47e</i>				
Orbital Period, P [days]	0.789592	±	0.000012	B
Radius Ratio, (R_P/R_\star)	0.01461	±	0.00013	B
Scaled semi-major axis, a/R_\star	3.205	±	0.014	B
Orbital inclination, i [deg]	85.98	±	0.75	B
Transit impact parameter, b	0.224	±	0.041	B
Time of Transit t_t [BJD _{TDB}]	2457011.34861	±	0.00033	B
Transit Duration t_{14} [hours]	1.899	±	0.013	B
RV Semi-amplitude K_e [m s^{-1}]	4.61	±	0.44	D
$M_P [M_\oplus]$	6.83	±	0.66	A,D
$R_P [R_\oplus]$	1.810	±	0.027	A,B
Surface Gravity [m s^{-2}]	20.5	±	2.0	A,B,D
Mean Density [g cm^{-3}]	6.35	±	0.64	A,B,D
<i>WASP-47b</i>				
Orbital Period, P [days]	4.1591289	±	0.0000042	B
Radius Ratio, (R_P/R_\star)	0.10193	±	0.00021	B
Scaled semi-major axis, a/R_\star	9.702	±	0.044	B
Orbital inclination, i [deg]	88.98	±	0.20	B
Transit impact parameter, b	0.173	±	0.032	B
Time of Transit t_t [BJD _{TDB}]	2457007.932132	±	0.000021	B
Transit Duration t_{14} [hours]	3.5722	±	0.0030	B
RV Semi-amplitude K_b [m s^{-1}]	140.64	±	0.44	D
$M_P [M_\oplus]$	363.1	±	7.3	A,D
$R_P [R_\oplus]$	12.63	±	0.15	A,B
Surface Gravity [m s^{-2}]	22.33	±	0.27	A,B,D
Mean Density [g cm^{-3}]	0.993	±	0.021	A,B,D
<i>WASP-47d</i>				
Orbital Period, P [days]	9.03077	±	0.00017	B
Radius Ratio, (R_P/R_\star)	0.02886	±	0.00016	B
Scaled semi-major axis, a/R_\star	16.268	±	0.074	B
Orbital inclination, i [deg]	89.32	±	0.23	B
Transit impact parameter, b	0.192	±	0.065	B
Time of Transit t_t [BJD _{TDB}]	2457006.36931	±	0.00039	B
Transit Duration t_{14} [hours]	4.288	±	0.039	B
RV Semi-amplitude K_d [m s^{-1}]	3.93	±	0.43	D
$M_P [M_\oplus]$	13.1	±	1.5	A,D
$R_P [R_\oplus]$	3.576	±	0.046	A,B
Surface Gravity [m s^{-2}]	10.1	±	1.1	A,B,D
Mean Density [g cm^{-3}]	1.58	±	0.18	A,B,D
Eccentricity	< 0.014			E
<i>WASP-47c</i>				
Orbital Period, P [days]	588.5	±	2.4	D
Time of Inferior Conjunction t_t [BJD _{TDB}]	2457763.4	±	4.9	D
$M_P \sin i [M_\oplus]$	398.2	±	9.3	A,D
Eccentricity	0.296	±	0.017	D
Argument of Periastron [degrees]	112.4	±	4.8	D
Semimajor Axis [AU]	1.393	±	0.014	A,D

NOTE. — A: Parameters come from our stellar parameter analysis in Section 3.3. B: Parameters come from analysis of the K2 light curve in Section 3.2. C: Parameters come from weighted average of spectroscopic parameters from three different methods described in Section 3.1. D: Parameters come from our radial velocity analysis in Section 3.4. E: The eccentricity of WASP-47 d was fit with a strong Gaussian prior of 0 ± 0.014 from TTV and dynamical stability arguments. The argument of periastron was not constrained in our fits either by the data or prior.